Case Studies in Thermal Engineering 10 (2017) 499–516

Contents lists available at ScienceDirect

Case Studies in Thermal Engineering

journal homepage: www.elsevier.com/locate/csite

# Natural convective heat transfer in a walled CCPC with PV cell

W. Li[a], M.C. Paul[b,*], N. Sellami[c], T.K. Mallick[d], A.R. Knox[b]

[a] School of Mathematics & Statistics, University of Glasgow, Glasgow G12 8QW, UK
[b] School of Engineering, University of Glasgow, Glasgow G12 8QQ, UK
[c] School of Engineering, Robert Gordon University, Aberdeen AB10 7JG, UK
[d] The Environment and Sustainability Institute, University of Exeter, Penryn TR10 9FE, UK

ARTICLE INFO

*Keywords:*
Crossed compound parabolic concentrator
Photovoltaic cell
Natural convective heat transfer
Nusselt number
Solar energy
CFD

ABSTRACT

The natural convective heat transfer phenomenon in an isolated, walled CCPC with PV cell is studied experimentally at 1000 W/m$^2$ irradiance and 28.5 °C ambient temperature as well as 0°, 10°, 20°, 30° and 40° incidences in indoor laboratory by using solar simulator. Then a series of numerical simulations are launched to estimate the CCPC natural heat transfer behaviour and optical performance based on steady heat transfer and laminar flow models with grey optical option. It is identified that the heat transfer and optical performances of CCPC are dependent on the incidence. Especially, the PV cell is subject to the highest temperature at an incidence less than 20°, and otherwise the top glass cover is with the highest temperature. The predicted temperatures, Nusselt numbers and heat loss ratios are consistent with the experimental observations basically, especially at the incidence less than 20° with (−10.1∼+3) % error in temperature, (−35.6∼+12.6) % in Nusselt number, and (−1.2∼+20.5) % in CCPC wall heat loss ratio. The optical parameters predicted agree very well with the measurements. The heat loss from the CCPC walls accounts for nearly 60% of the total incoming solar irradiance and should be paid significant attention in the design of CCPC.

## 1. Introduction

Compound parabolic concentrators (CPCs) are a sort of optical devices applied for solar energy collection to augment solar energy utilisation. Since 1970s CPCs have experienced an extensive development. Presently, CPCs can be in three-dimensional shape, namely a polygonal aperture, and it is shown that a squared CPC or crossed compound parabolic concentrator (CCPC) has good optical performance and lower cost [1–3]. Thus, air-filled CCPCs can potentially find significant applications in solar energy in the future.

Thermal performance or heat loss of a CCPC is equally important compared with its optical behaviour. For example, if an air-filled CCPC is integrated into a photovoltaic (PV) module, the CCPC should be designed with high natural convective heat transfer coefficient to discharge the heat generated by the PV cells efficiently to the ambient air and maintain the cells in a low temperature. Otherwise, if an air-filled CCPC is combined with a PV/thermal (PV/T) module, it should have a low natural convective heat transfer coefficient to allow the water in the heat exchangers to extract heat as much as possible from the cells.

There are many studies on natural convective heat transfer in CPCs done experimentally and numerically. In [4], natural convective heat transfer coefficients of a series of V-shaped troughs were measured when the Rayleigh number of filled air in the troughs was up to $10^7$ and the tilt angle was varied in 30°−90° and the concentration ratios (*CR*) were 2, 3, 4 and 5. The Nusselt number has been correlated to the Rayleigh number, *CR* and tilt angle. In [5], natural convective heat transfer in three line-axis CPCs (*CR* = 4.13,

* Corresponding author.
*E-mail address:* Manosh.Paul@Glasgow.ac.uk (M.C. Paul).

http://dx.doi.org/10.1016/j.csite.2017.10.009
Received 2 May 2017; Received in revised form 6 October 2017; Accepted 16 October 2017
Available online 20 October 2017

2.67 and 1.56) was experimented by making use of a Mach-Zehnder interferometer at 0°, 10°, 20° and 30° tilt angles. The Nusselt number has been correlated to CPC geometrical parameter, tilt angle and the Grashof number. Energy balance experiments were carried out on a line-axis CPC in [6], showing a polyester anti-convective surface covered on top of the cylindrical absorber that prevented the natural heat convection in the CPC enclosure by reducing the thermal loss from it. Heat loss measurements were conducted on a V-trough collector with $CR = 1.56$ and aluminium laminate reflector at 45° tilt angle in [7]. It was identified that the baffles could reduce the thermal loss by 20%, and the heat loss from the reflector covered by Teflon was less than 20% compared with the case without Teflon.

The Nusselt number correlations for natural convective heat transfer in rectangular enclosures with various aspect ratio and tilt angles were reviewed in [8]. A series of experiments on three line-axis CPCs at different tilt angles were made and Nusselt number was extracted to characterise the natural convective heat loss from the absorber plate and correlated to the Rayleigh number, two tilt angles, height of CPC, two aspect ratios and water temperature at the inlet of heat exchanger in [9]. The natural convective heat transfer in a V-trough concentrator by heating the bottom of the trough was performed in [10] and a relation between the Nusselt number and the Rayleigh number was worked out when the Rayleigh number is in the range of $4\times10^7 - 1\times10^8$ for the specific V-trough concentrator.

Besides forgoing experimental investigations, significant attention has been paid on the numerical studies of the natural convective heat transfer in CPC enclosures since 1990s. In [11], a unified 2D model for optics and heat transfer in line-axis CPC was proposed, and validated with experimental measurements. In the model, solid and fluid domains were unified. The thermal model, rays trace with reflection, absorption and emitting, fluid flow and heat conduction were coupled, but the absorption and heat conduction were treated in a slightly simple manner. The unified model has been applied in the optical and natural heat transfer analysis in CPC cavity [12–17]. In particular, based on the predicted results at different geometrical parameters (height and half-width of CPC), tilt angles and Grashof numbers, a new Nusselt number correlation was proposed for the heat transfer in the cavity.

The natural convective heat transfer in line-axis CPCs was analysed by using a 2D vorticity-stream function formulation based on a Navier-Stokes solver in [18]. The internal and external radiation effects were considered in the computational models. The influences of *CR*, internal bafflers attached to the cover and absorber surface, filled gas in the CPC enclosure on the collector efficiency were clarified numerically. These means could improve the collector efficiency by 30% compared with reference case.

The natural convective heat transfer in a line-axis CPC cavity was investigated numerically via 2D and 3D models by using ANSYS 14.0 CFX and internal radiation was handled with face-to-face model in [19]. The predicted air velocity in the CPC enclosure and the temperature on the CPC walls and top glass cover were compared with PIV and thermocouples measurements. It was found that 86% heat loss was released from the absorber tube surface, 73% of this loss was discharged out of the CPC from the top glass cover.

In comparison with CPCs, a very little attention has been paid to natural convective heat transfer in CCPC enclosures so far. A CCPC was built and integrated with a PV cell to form a PV module with CCPC in [20]. Then, the optical, electric performance and temperature on the bottom cover were measured, but the natural convective heat transfer in the CCPC cavity was ignored. A simulation of natural heat transfer and optical performance in a CCPC with PV cell was conducted in [21]. It was identified that the PV cell was subject to the highest temperature if the incident angle was less than 30°; otherwise, the top glass cover was with the highest temperature. Note that in the simulation the CCPC was just with reflective film and without wall thickness, thus CCPC wall effect on the heat transfer has been excluded. The temperature on a walled CCPC with PV cell was measured in indoor laboratory and simply compared with the results predicted by using ANSYS CFX 15.0 in [22].

The aim of the present work is to characterise the natural convective heat transfer behaviour in a CCPC cavity experimentally and numerically and provide a guide for the CCPC design of a PV/T module which is linked to the ongoing project SUNTRAP (scalable solar thermoelectrics and photovoltaics) for potentially achieving an overall increased utilisation efficiency of solar energy.

Note that a CCPC with PV cell is subject to multiphysics effects, including optics, solar radiation, conductive and convective heat transfer and solar cell electronics. Initially, we ignore solar cell electronic phenomenon and put an emphasis on the coupled optics, solar radiation, conductive and convective heat transfer.

We measure the temperature on the top glass cover of an air-filled, walled CCPC proposed in [3], in the monocrystalline PV cell and on the bottom glass cover of the PV cell at 0°, 10°, 20°, 30° and 40° tilt/incident angles in an indoor laboratory. Then the optical performance and natural convective heat transfer are simulated by making use of ANSYS 15.0 CFX based on a coupled solar radiation, conductive heat transfer in solid domains and convective heat transfer in fluid domain. The Nusselt number of CCPC is obtained and heat loss features in the CCPC cavity are clarified.

## 2. Thermal experiments

### 2.1. Geometry of CCPC and PV cell

An air-filled CCPC was designed and its optical performance was characterized by using a 3D ray trace in-house code [20]. Subsequently, this CCPC was incorporated into a 9 × 9 CCPC module to manufacture a PV module. Except the CCPC, the PV module consists of a top glass cover, a PV cell (two-layer sylgard elastomer and a doped silicon layer in between) and a bottom glass cover. The module was illuminated by a solar simulator in an indoor laboratory with 1000 W/m$^2$ uniform radiation intensity and 25 °C ambient temperature under various incidences in [20]. For the PV module, the electrical performance and temperature on the bottom glass cover were measured and sampled. We isolate one CCPC from the module and consider it as a physical model for our experiment, and multiphysics simulation, see Fig. 1, where the profile of the CCPC is provided [3]. The layer thickness of the solar cell is taken from [23].

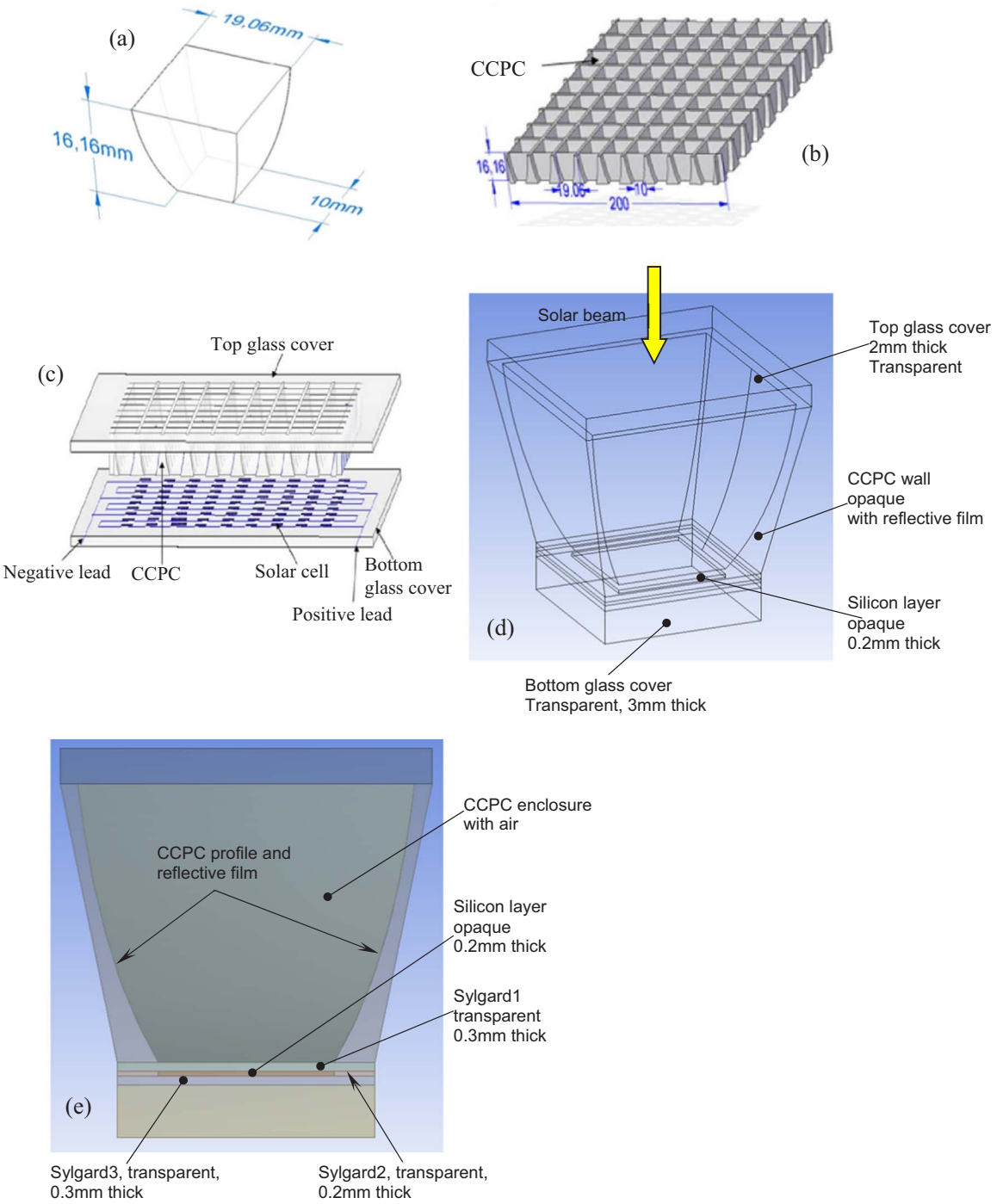


**Fig. 1.** CCPC model with PV cell, (a) CCPC profile, (b) 9×9 CCPC module, (c) PV module for experiment [20], (d) isolated CCPC with PV cell from the module, (e) a mid-span cross-sectional view of the isolated CCPC, (a) from [3], (b) and (c) from [20].

3D ray trace method is an approach for calculating the path of photo waves through a system composed of a few components by considering refection and absorption characteristics on surfaces of the components. The method provides an approximate solution to the Maxwell's equations. The 3D ray trace code using MATLAB has been developed specifically for the case of the CCPC in [3]. The code is written in the way that the incident rays entering the CCPC face in two situations; they either hit the exit aperture without reflection or hit one of the side walls to be reflected. After the first reflection, the incident ray will face three situations: exit the CCPC from the entry aperture and disappear, hit another or the same side wall to be reflected yet again, or reach the exit aperture. The ray is followed until it either reaches the exit aperture where the PV cells are placed or exits the CCPC from the entry aperture and

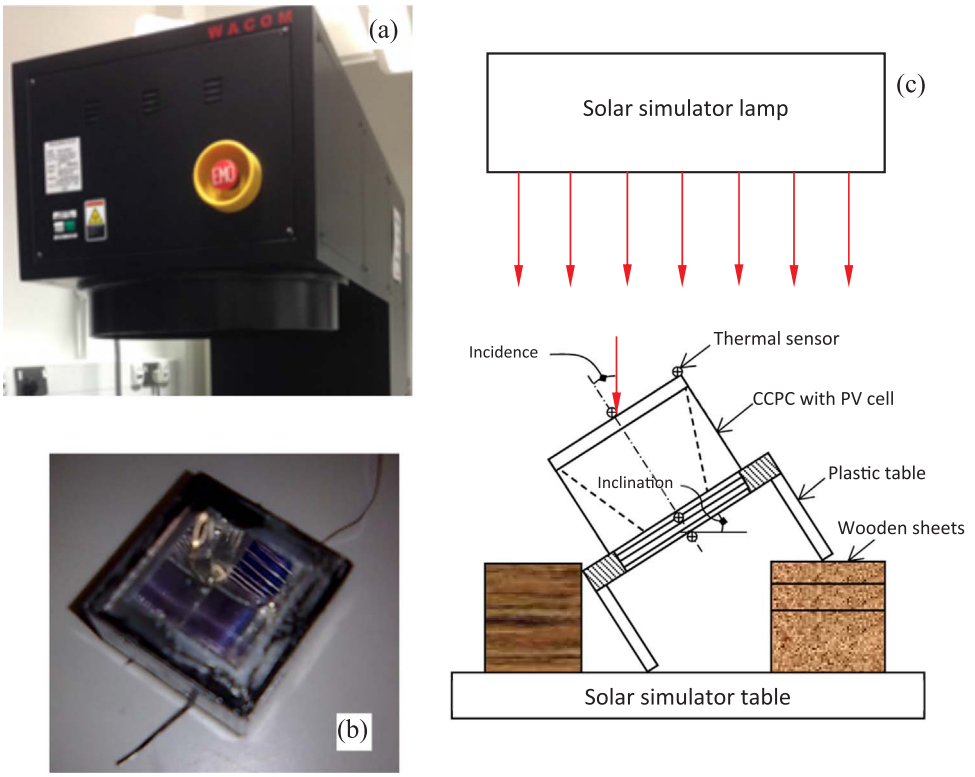


**Fig. 2.** WXS-210S-20 solar simulator (a), a picture of the CCPC with PV cell (b) and a position of the CCPC in experiment (c), note that (c) is not in real scale, the thermal sensors are positioned in the centre of the surface of the top glass cover, PV cell and bottom glass cover and the middle of the edge of CCPC.

vanishes into space.

### 2.2. Experimental apparatus and results

A series of natural convective heat transfer experiments on the CCPC with PV cell were conducted in the indoor PV laboratory in the Environment and Sustainability Institute at the University of Exeter, Penryn, England. The CCPC and PV cell are the same those used in the simulation hereby as shown in Fig. 2. Four thermal sensors are fixed in the top glass cover centre and edge, bottom cover centre and the silicon layer of the cell, respectively. Four channel of Model 27000 Multimeter/Data Acquisition System produced by Keithley Co. Ltd are activated via XLINX software to connect those sensors and allow temperature data to be collected. The CCPC model without electrical connections is illuminated under a solar simulator (WXS-210S-20, AM1.5 G, made by Wacom Electric Co. Ltd, Japan). A natural heat transfer experiment needs to last for 45–60 min to get a steady state. In this period, the indoor air ambient temperature rises to 29 °C from 28 °C. The simulator illumining beam is unmovable and remains downwards all the time and the top glass cove is faced against the beam.

The CCPC model is fixed onto a small plastic table. The squared through hole on the table surface accommodates and holds the CCPC model, allowing it can be subject to free convective condition over its outside surfaces, see Fig. 2(c). The orientation of the CCPC model is adjusted by tilting the table two legs in one side with certain thick wooden sheets to achieve desirable incidences, such as 0°, 10°, 20°, 30° and 40°.

The temperature-time history curves are illustrated at various incidences in Fig. 3. The temperature in the top glass cover, PV cell (silicon layer) and bottom cover is dependent on incidence. Further, it is observed that the PV cell is subject to the highest temperature, while the top glass cover centre is in the lowest temperature, if the incidence is less than 30°. The temperatures in the bottom glass cover and the top glass cover edge are in between. If the incidence is at 40°, the temperatures in the top glass cover, PV cell and bottom glass cover are close to each other. In [24,25], the cell temperatures of flat PV modules were measured at 0° incidence. Our temperature measurements at the same incidence are consistent with these observations.

The transient Nusselt number on the bottom of CCPC has been extracted based on the lumped heat transfer model in [26,27]. The Nusselt number is illustrated in Fig. 4, which defined by the convective heat transfer coefficient, $h$, cell temperature, $T_{cell}$, film temperature, $T_f$, air thermal conductivity, $k$, and CCPC cavity height, $H$, i.e.

$$Nu_b = \frac{h(T_{cell} - T_f)}{\frac{k(T_{cell} - T_f)}{H}} = \frac{hH}{k} \tag{1}$$

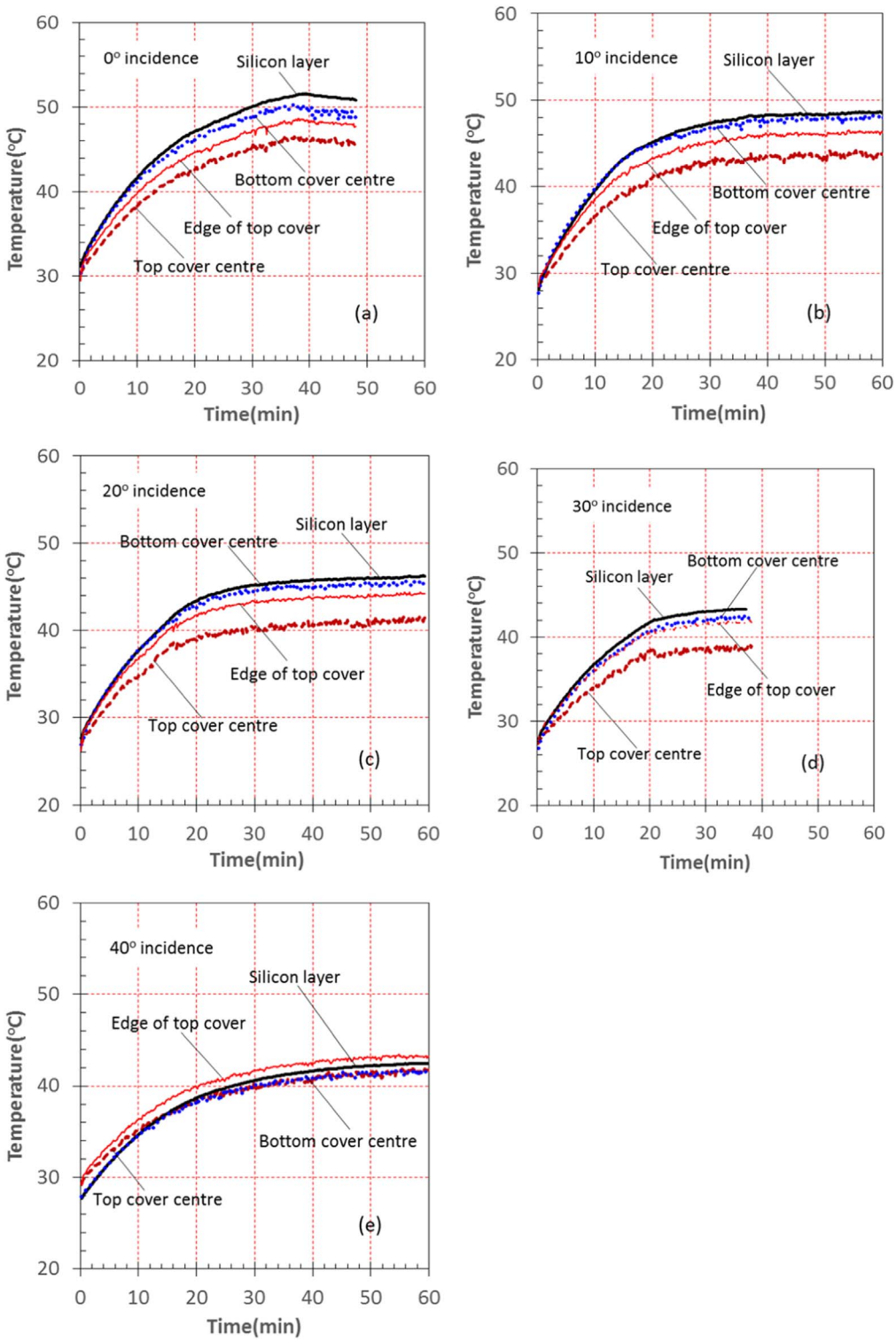


**Fig. 3.** Measured temperature-time history curves at incidences 0°, 10°, 20°, 30° and 40°.

where $T_{cell}$ is measured in the heat transfer experiments in °C, $T_f$ is the mean air temperature in the CCPC cavity in °C, estimated with the measured cell temperature, two measured temperatures in the glass cover centre and the edge, $T_{gc}$ and $T_{ge}$, $T_f \approx 0.5[T_{cell} + 0.5(T_{gc} + T_{ge})]$, the CCPC cavity height, $H = 16.16$ mm, the thermal conductivity depends on $T_f$, $k = 0.02624[(T_f + 273.15)/300]^{0.8646}$, W/(m$^2$ K). Since the temperature depends on incidence, the Nusselt number is related to the

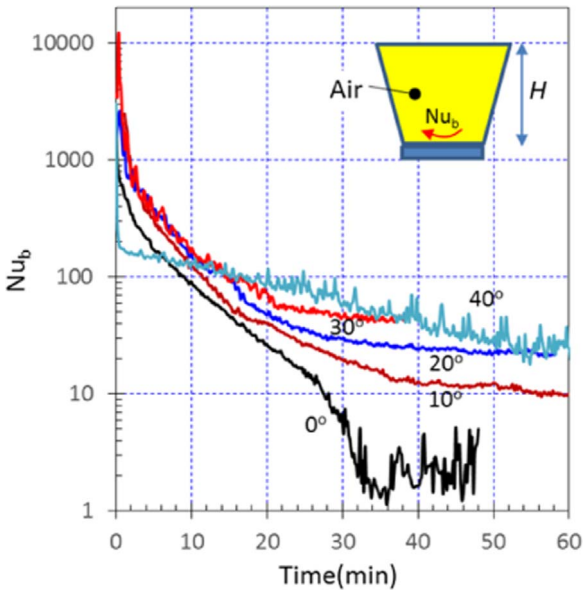


**Fig. 4.** Transient Nusselt number of natural convection heat transfer in the bottom of CCPC at various incidences, the numerical figures alongside the curves are experimental incidence.

incidence as well. The fluctuation in temperature results in a bumpy Nusselt number profile when time is over 30 min at 0° incidence.

The Rayleigh numbers in the steady state are 7207.6, 6638.9, 5932.2, 5060.8 and 5649.6 at 0°, 10°, 20°, 30° and 40° incidences; meanwhile the Grashof numbers are 10,263.6, 9448.8, 8437.5, 7192.4 and 8244.7, respectively. The Rayleigh number is defined by the following

$$\mathrm{Ra} = \frac{g\beta \mathrm{Pr}\rho^2 H^3 (T_f - T_a)}{\mu^2} \tag{2}$$

where the gravity acceleration is $g = 9.81\ \mathrm{m/s^2}$, the air thermal expansion coefficient is $\beta = 1/(T_f + 273.15)\ \mathrm{K^{-1}}$, the air temperature during the thermal experiments is $T_a = 28.5\ ^\circ\mathrm{C}$, $\rho$ and $\mu$ are the air density and dynamic viscosity at $T_a = 28.5\ ^\circ\mathrm{C}$, Pr is the Prandtl number at $T_a = 28.5\ ^\circ\mathrm{C}$, $\mathrm{Pr} = 0.7071$.

Based on Fig. 4, the steady Nusselt numbers are 5.0, 10.1, 21.4, 42.6, and 22.6. From Fig. 11 in [9], the Nusselt numbers interpolated by using the Rayleigh numbers mentioned are in the range of 2.0–15.0 at 0° incidence. This suggests that the experimental Nusselt numbers here at 0° and 10° are consistent with this range.

## 3. Numerical simulations

### 3.1. Governing equations

Multiphysics simulations of the walled CCPC with PV cell are based on the governing equations of optics in both the solid and fluid domains, conductive heat transfer in the solid domains and natural convective heat transfer in the fluid domain,.i.e. the enclosure of the CCPC where an air flow occurs. These governing equations can be found in [28,29], and they have been summarized in Appendix A. The natural conductive heat transfer outside the CCPC is not solved together with the conductive heat transfer in the CCPC walls, instead, it will be considered with constant heat flux boundary condition at a constant ambient temperature.

### 3.2. Material properties, boundary conditions and numerical methods

#### 3.2.1. Material properties

The optical, thermal and radiative properties of the materials used in the optical and thermal models at 25 °C are listed in Table 1. The property parameters include density, specific heat capacity, thermal conductivity, absorption coefficient, scattering coefficient, refractive index, emissivity and diffuse fraction. The grey radiation model is redeemed in the paper, thus the absorption coefficient, emissivity and refractive index are independent of wavelength and remain to be constant.

Additionally, when the solar beam propagates in the media, it is absorbed without any scattering effect; when it is reflected on a boundary, there is no diffuse. Therefore all the scattering coefficient and diffuse fraction are set to be zero in the table.

#### 3.2.2. Boundary conditions

Four kinds of boundary condition are composed in the walled CCPC optical and heat transfer analysis, see Fig. 1(d) and (e). The

**Table 1**
Thermal and radiative properties of glass, air, syldard, silicon and reflective film at 25 °C.

| Medium | Glass | Air | Sylgard1,2,3 | Silicon | CCPC wall |
|---|---|---|---|---|---|
| Density, $\rho$(kg/m$^3$) | 2500 | 1.185 | 1030 | 2330 | 2702 |
| Specific capacity, $c_p$(J/(kg K)) | 750 | 1004 | 1100 | 712 | 903 |
| Thermal conductivity, $k$(W/(m K)) | 1.4 | 0.0261 | 0.16 | 148 | 237 |
| Absorption coefficient, $\alpha$(m$^{-1}$) | 2 | 0.01 | 2 | 70,000 | 67 |
| Scattering coefficient, $\gamma$ | 0 | 0 | 0 | 0 | 0 |
| Refractive index, $n$ | 1.47 | 1.0 | 1.42 | 4 | 2.23 |
| Emissivity, $\varepsilon$ | 0.94 | 0 | 0.9 | 0.672 | 0.06 |
| Diffuse fraction | 0 | 0 | 0 | 0 | 0 |

first is the interface between the solid domain and fluid or other solid domain; the second is the boundary condition that is subject to natural convective heat transfer with a certain heat transfer coefficient; the third is the boundary condition that can emit radiation; and the last one is the boundary condition that can receive the solar radiation. These boundary conditions are detailed in Table 2.

On the top glass cover, the upper surface is subject to a 1000 W/m$^2$ uniform radiation intensity whose incidence can be set to 0°, 10°, 20°, 30° and 40° in the west-east plane, respectively. In CFX, this intensity is imposed to be a boundary source to drive the whole heat transfer process in the CCPC with PV cell, see Fig. 5(a). The one part of the bottom surface of the cover is the interface between the cover and the filled air, and the heat and radiation fluxes are conserved across it. The other part is the interface with the CCPC walls. The other surfaces are subject to natural convective heat transfer with a heat transfer coefficient of 10 W/(m$^2$ K) and emitting with an emissivity of 0.94.

For the CCPC, there are three interfaces; the first interface is with the top glass cover, the second one is with Sylgard1 layer, and the last one is with six surfaces of the filled air. On the rest four boundaries, there is a natural convective boundary condition with a heat transfer coefficient of 10 W/(m$^2$ K) and an emissivity of 0.06.

For Sylgard1 layer, there are two interfaces, one is with the air and one is with the PV cell. The PV cell is subject to three interfaces, namely, the interface with Sylgard1 layer, the interface with Sylgard2 layer and the interface with the Sylgard3 layer. The Sylgard3 layer has two interfaces, one with the PV cell and one with the bottom glass cover. The four side surfaces of the Sylgard1, Sylgard2 and Sylgard3 layers as well as the five surfaces of the bottom cover are subject to a natural heat transfer coefficient of 10 W/(m$^2$ K) and their own emissivity, as shown in Table 1, respectively.

Here, the free convective heat transfer coefficient over the outside surfaces of the walled CCPC model is predicted by using the well-known correlation: $h = 5.7 + 3.8V_{wind}$ in solar energy engineering in [30]. During the thermal experiments, an air conditioner was in operation to maintain the ambient temperature at a certain level, say 28.5 °C, in the indoor laboratory in July in Penryn. We

**Table 2**
Boundary conditions for isolated walled CCPC with PV cell.

| Domain | Interface | Natural convection | Emitting | Boundary source |
|---|---|---|---|---|
| Top glass cover | Bottom surface | Top surface<br>Four side surfaces<br>Heat transfer coefficient 10 W/(m$^2$ K) | Top surface<br>Four side surfaces | Top surface for sunlight in various incidences |
| CCPC side wall | Top surface, four inner surfaces<br>Bottom surface | Four side surfaces<br>Heat transfer coefficient 10 W/(m$^2$ K) | Four side surfaces | N/A |
| Filled air | Six surfaces | N/A | N/A | N/A |
| Sylgard1 layer | Top surface<br>Bottom surface | Four side surfaces<br>Heat transfer coefficient 10 W/(m$^2$ K) | Four side surfaces | N/A |
| Silicon layer | Top surface<br>Bottom surface | Four side surfaces<br>Heat transfer coefficient 10 W/(m$^2$ K) | Four side surfaces | N/A |
| Sylgard2 layer | Inside surfaces with silicon layer side surfaces | N/A | N/A | N/A |
| Sylgard2 layer | Top surface<br>Bottom surface | Four side surfaces<br>Heat transfer coefficient 10 W/(m$^2$ K) | Four side surfaces | N/A |
| Sylgard3 layer | Top surface<br>Bottom surface | Four side surfaces<br>Heat transfer coefficient 10 W/(m$^2$ K) | Four side surfaces | N/A |
| Bottom glass cover | Top surface | Bottom surface<br>Four side surfaces<br>Heat transfer coefficient 10 W/(m$^2$ K) | Bottom surface<br>Four side surfaces | N/A |

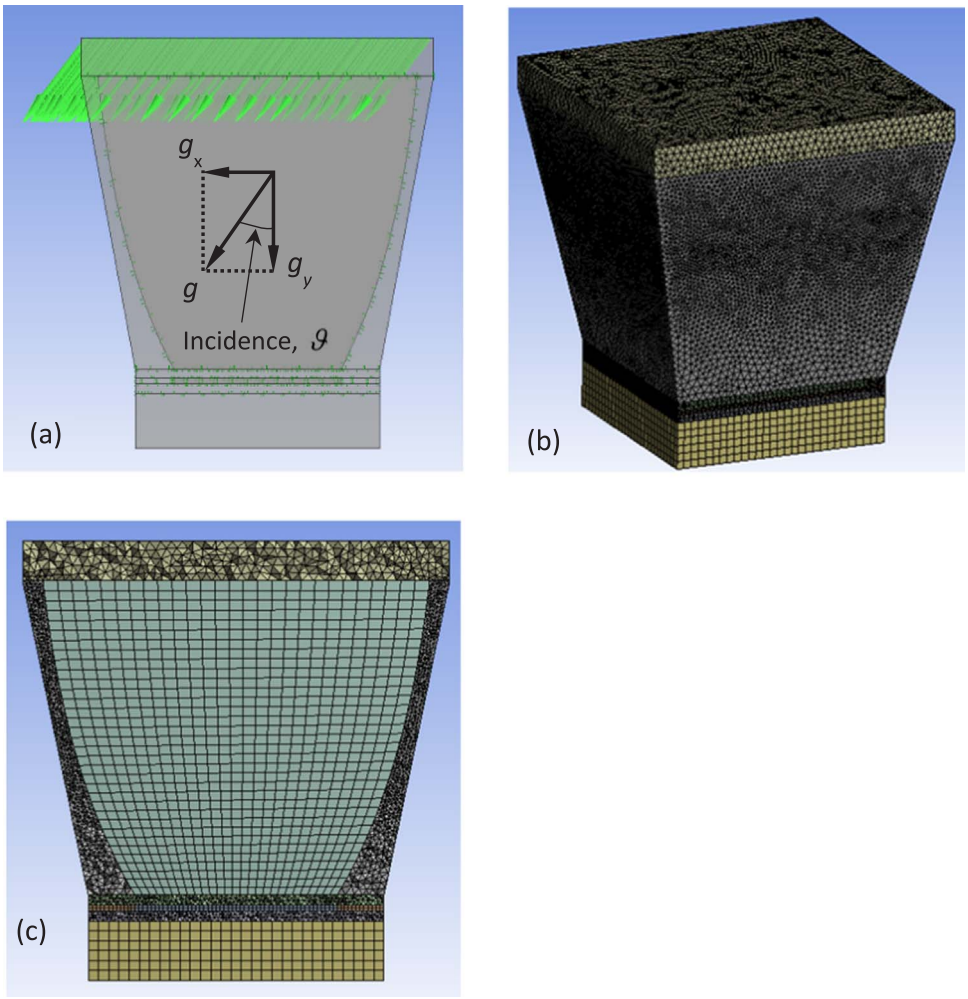


**Fig. 5.** Orientations of the walled CCPC with PV cell in thermal experiment and multiphysics simulation and the mesh generated in the domains, (a)orientation of the CCPC in simulation and gravity acceleration decomposition, (b) mesh in the domains, (c) a mid-span cross-sectional view of mesh, the lines with arrows represent the solar irradiance orientation applied.

assume the air velocity issued from the conditioner is 1 m/s in the room, resulting in a free convective heat transfer coefficient $h = 5.7 + 3.8 \times 1 = 9.5 \approx 10\ \mathrm{W/(m^2\ K)}$.

In the thermal experiments, the CCPC was tilted to a certain angle, as sketched in Fig. 2(c). In this situation, the air filled in the enclosure of CCPC is subject to a vertical acceleration of gravity. However, in a multiphysics simulation, the CCPC is placed horizontally without any inclination, as seen in Fig. 5(a). To mimic the experimental condition demonstrated in Fig. 2(c), the acceleration of gravity is tilted to the same angle to the incidence and has two acceleration components each in the vertical and horizontal directions, $g_x$ and $g_y$, i.e., $g_x = -g \sin \vartheta$, $g_y = -g \cos \vartheta$, where $\vartheta$ is the tilt angle or incidence, as shown in Fig. 5(a). Then $g_x$ and $g_y$ are input into CFX.

### *3.2.3. Meshing and numerical methods*

ANSYS mesh module was employed to generate two sets of mesh in the fluid and solid domains. A fair mesh in the fluid and solid domains was generated with $2 \times 10^{-4}$ m minimum mesh and proximity minimum sizes, $5 \times 10^{-4}$ m maximum mesh and face sizes, resulting in 261,991 nodes and 1072,215 tetrahedral (top glass cover, CCPC wall, Sylgard1 and Sylgard3) and hexahedral (air, PV cell, Sylgard2 and bottom glass cover) elements totally, see Fig. 5(b) and a mid-span cross-sectional view in Fig. 5(c). The mesh metric for element quality is in the range of 0.23–1.0 with a 0.85 mean value, showing a good mesh quality.

Moreover, a fine mesh with 843,462 nodes and 2822,199 tetrahedral (top glass cover, CCPC wall, Sylgard1 and Sylgard3) and hexahedral (air, PV cell, Sylgard2 and bottom glass cover) elements was generated with $1 \times 10^{-4}$ m minimum mesh and proximity minimum sizes, $5 \times 10^{-4}$ m maximum mesh and face sizes.

The laminar air flow and thermal analysis are solved based on finite volume method. A high resolution scheme discretizes the advection terms in the continuity, momentum and thermal energy equations. The maximum number of iterations taken is 8000, and the root mean square residual tolerance is $1 \times 10^{-6}$.

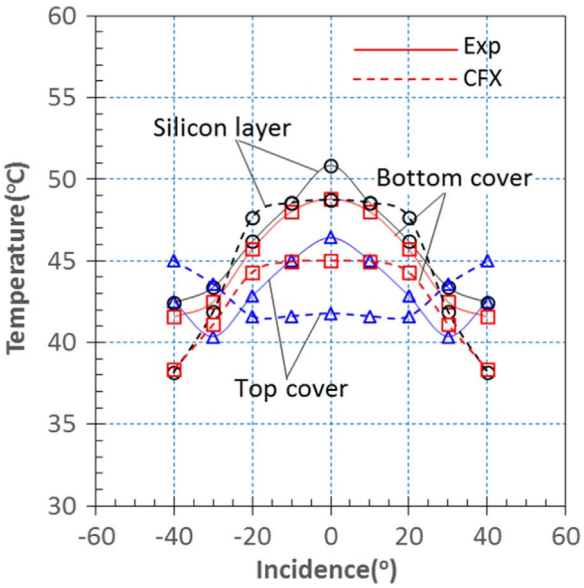


**Fig. 6.** Mean temperature of the top glass cover, PV cell (silicon layer) and the bottom glass cover versus incidence at steady state.

The Monte Carlo method is applied to solve solar beam propagation in the participating media: air, glass, sylgard, silicon with 200,000 no. of histories under 64 target coarsening rate and 20,000 no. of small coarse grid size. During a solution process, the thermal and radiation energy equations are coupled when the fluid flow governing equations are solved for each of the 30 iterations.

It was shown that in the fine mesh, the average temperature of the PV cell is increased by 0.01 °C and the average temperature of bottom glass cover is raised by 0.08 °C in comparison with that in the fair mesh, suggesting the fair mesh with 261,991 nodes and 1072,215 elements is reasonable and thus used in the following simulations.

### 3.3. Predicted temperature profiles

The steady average temperatures on the top glass cover, in the PV cell layer and on the bottom glass cover are compared with the experimental measurements in Fig. 6. The temperature in the PV cell and on the bottom cover is with 2–3 °C difference against the measurements at $0^\circ - 40^\circ$ incidences, showing good agreement in the temperature between prediction and measurement. For the top glass cover, this agreement is slightly poor. For an incidence in a range of $0^\circ - 20^\circ$, the predicted PV cell temperature differs from the measurement by $(-10.1 \sim +3)$ % error.

The measured temperatures in the PV cell and on the bottom glass cover decrease steadily with increasing incidence, but the temperature on the top glass cover rises with increasing incidence when the incidence is larger than 30°.

The predicted temperatures remain unchanged basically until the incidence is higher than 20° in these components. Once the incidence is beyond 20°, the temperature descends in the PV cell and on the bottom glass cover, but rises on the top glass cover, exhibiting a temperature rising effect there.

The temperature rising effect on the top glass cover is not observed in the experiments actually. This can be explained by the temperature contours on the top glass cover and the PV cell and bottom cover at 0°, 10°, 20°, 30° and 40° incidences, as shown in Fig. 7. The temperature is not uniform at all the incidences, and there is a 2–5 °C higher temperature spot on the top glass, its position and temperature difference depending on the incidence. The highest temperature does not increase until the incidence is larger than 20°. Contrarily, the temperatures in the PV cell and on the bottom glass cover always decrease with increasing incidence. Obviously, the intensified highest temperature spot on the top glass cover results in an increased temperature profile on the top glass cover at an incidence larger than 20°. It is understood probably due to the fact that the glass cover is regarded as an opaque material in CFX, and the energy transmitted through the glass depends on its absorption coefficient and the energy reflected to the air.

### 3.4. Predicted Nusselt number and heat loss ratio

The steady Nusselt numbers for the free convective heat transfer between the air-filled and Sylgrad1 layer, top glass cover, CCPC inside walls are calculated from the heat flux across these surfaces and their area, air film temperature and mean temperature of these surfaces as well as the CCPC height. The experimental and predicted Nusselt numbers and heat loss ratio in the steady state are demonstrated in Fig. 8(a) and (b). The Nusselt numbers are based on the height of CCPC and the heat loss ratio is defined as the heat loss from a CCPC surface exposed to the air over the total solar energy on the top glass cover.

Three Nusselt numbers, $Nu_b$, $Nu_w$ and $Nu_c$ depend on incidence and note that $Nu_c > Nu_b > Nu_w$ when the incidence is in $0^\circ - 20^\circ$. Also, the predicted Nusselt number, $Nu_b$, is in agreement with the experimental observation basically. Specially, the predicted Nusselt

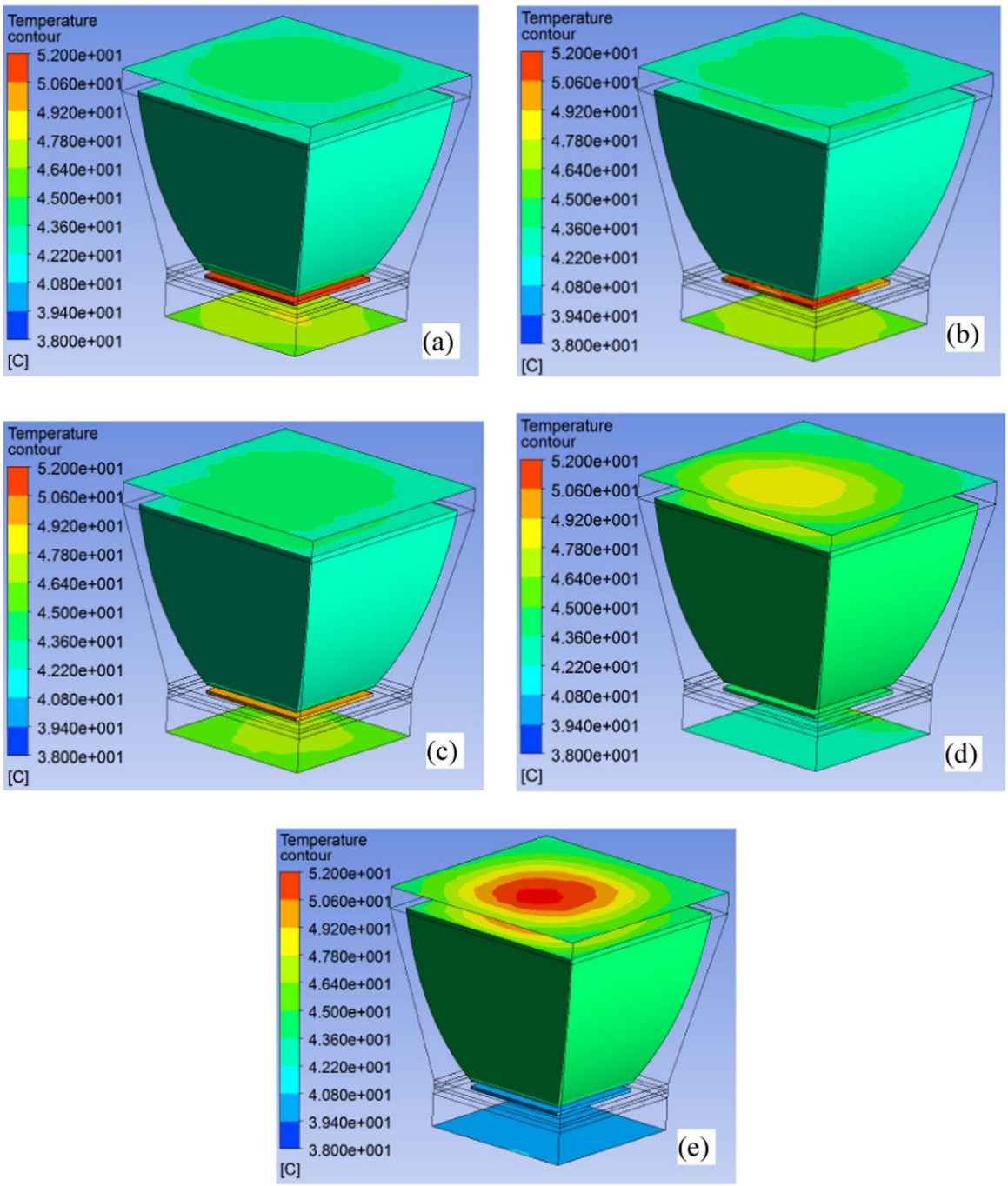


**Fig. 7.** Temperature contours on the top glass cover, PV cell and bottom glass cover at (a) 0°, (b) 10°, (c) 20°, (d) 30° and (e) 40° incidences, respectively.

number $Nu_b$ is in $(-35.6\sim+12.6)$ % error compared with the Nusselt number based on the measured temperatures.

The heat loss from the CCPC mainly occurs on the CCPC walls, but the heat loss from the top glass cover is comparable to that from the bottom glass cover. This implies that the CCPC wall should be treated carefully in design, insulation and material selection. Note that the predicted heat loss ratio across the CCPC walls differs from the that based on the measured temperature by an error in the range of $(-1.2\sim+20.5)$ %.

Heat flow direction and relative magnitude, $Q_c/E_t$ $Q_b/E_t$ and $Q_w/E_t$, are illustrated in Fig. 8(c), in which $Q_c$, $Q_b$ and $Q_w$ are the heat through the glass cover, bottom cover, and CCPC walls, respectively, $E_t$ is the total incoming energy. The $Q_c$ direction is towards, but the $Q_w$ is outwards the air cavity at any incidence. The $Q_b$ direction is towards the air cavity at a smaller incidence in a range of $0^\circ-20^\circ$, while it is off the cavity when the incidence is larger than 20°. This variation pattern of heat flow direction reflects the

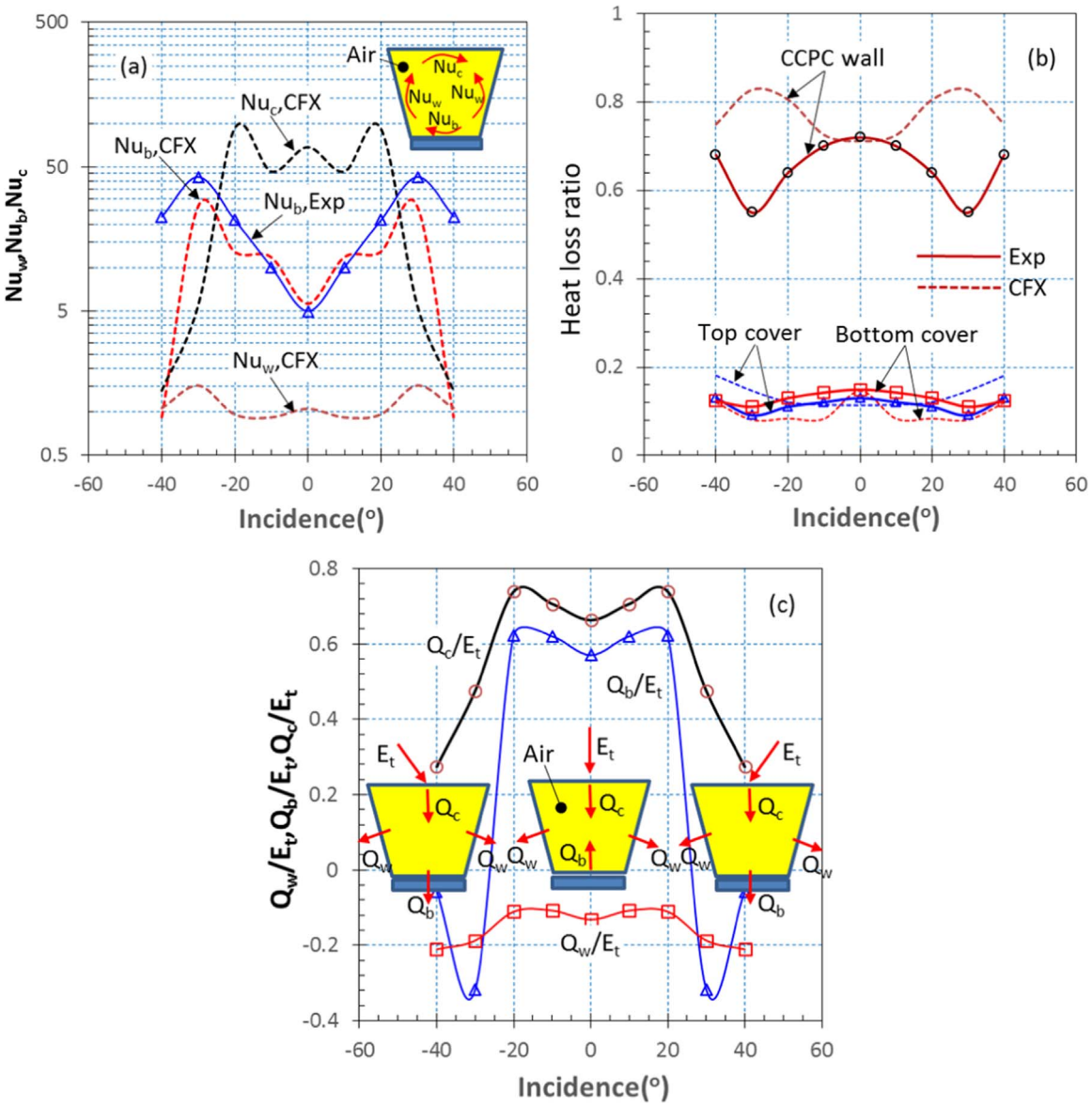


**Fig. 8.** Experimental and predicted Nusselt numbers (a), heat loss ratio (b) and thermo-flow (c) in the steady state, the numbers are based on the height of CCPC, and the heat loss ratio is defined as the heat loss from a CCPC surface exposed to the air over the total solar energy on the top glass cover, $Q_c$, $Q_b$ and $Q_w$ are the heat through the top glass cover, bottom cover and CCPC wall, $E_t$ is the total incoming energy.

highest temperature position change from the PV cell to the top glass cover with increasing incidence as shown in Fig. 7.

### 3.5. Predicted flow pattern in CCPC enclosure

The velocity vectors of the filled air in the CCPC enclosure at 0°, 10°, 20°, 30° and 40° incidences are illustrated in Fig. 9. At 0° incidence, the air initially rises upwards from the bottom of the cavity in the central zone until arriving at the bottom of the top glass cover, then it moves along the glass surface outwards and goes down along the CCPC side walls. Finally, it reaches the bottom of the cavity and flows inwards until meeting in the cavity central area, where it goes up again. As a consequence, a vortex-loop is generated in the cavity and the highest velocity zone remains in the cavity centre. Even though this vortex-loop can remain to exist at 10° and 20° incidences, the rising air stream has been away from the central line of the CCPC cavity.

When the incidence increases up to 30°, the vortex-loop pattern mentioned above no longer exists, and changes into a single vortex pattern in the vertical plane due to the transverse acceleration component of gravity and the temperature gradient from the top cover to the PV cell.

The maximum air velocity is related to incidence and in the range of 2.5–10.0 mm/s. At 0° incidence, the maximum velocity in the

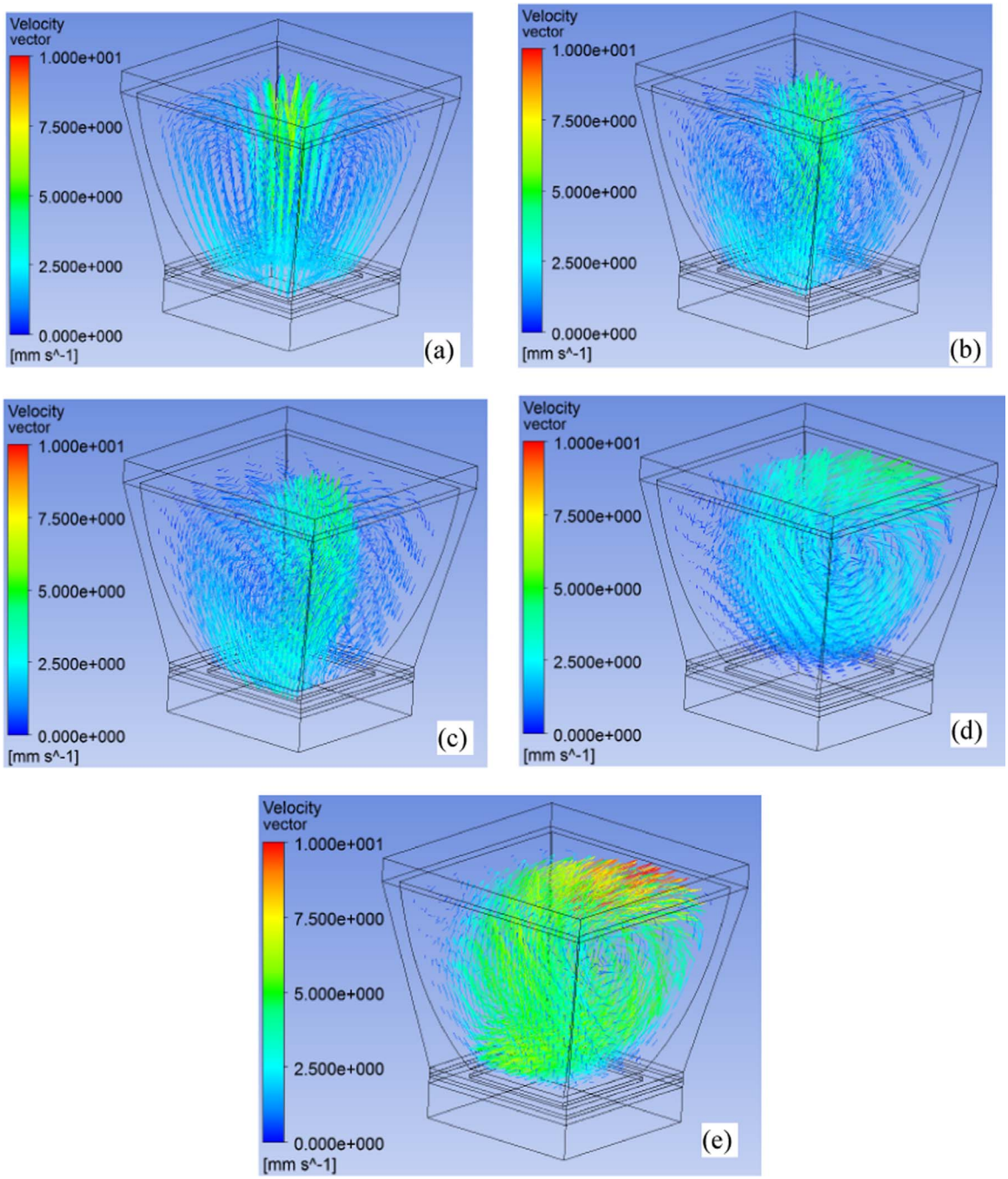


**Fig. 9.** Velocity vector of the air-filled in the CCPC enclosure at (a) 0°, (b) 10°, (c) 20°, (d) 30° and (e) 40° incidences, respectively.

middle of CCPC cavity, with the increasing incidence, however, it moves to a position close to the top glass cover. As a result, Reynolds number of the air flow, which is based on the maximum velocity, density and dynamic viscosity of the air at 25 °C and 16.16 mm CCPC height, is varied from 7.05 to 14.1.

### *3.6. The highest temperature core predicted in PV cell at small incidence*

In Fig. 7(a) to (c), a highest temperature core in the PV cell (silicon layer) is shown when the incidence is at 0°, 10° and 20°. To fully understand the mechanism for the occurrence of the highest temperature core in the cell, the intensity ratio of transmitted to incident solar radiation in each medium of the CCPC is estimated by making use of the Beer-Lambert law [31] below and presented in Table 3.

**Table 3**
Intensity ratio of transmitted and incident radiation through media.

| Medium | Absorption coefficient $\alpha(m^{-1})$ | Thickness $l$(mm) | Intensity ratio $I/I_0$ |
|---|---|---|---|
| Top glass cover | 2 | 2 | 0.9960 |
| Air in chamber | 0.01 | 16 | 0.9998 |
| Top sylgard layer | 2 | 0.3 | 0.9994 |
| PV Silicon layer | 70,000 | 0.2 | $8.3153 \times 10^{-7}$ |
| Bottom sylgard layer | 2 | 0.3 | 0.9994 |
| Bottom glass cover | 2 | 3 | 0.9940 |

$$I/I_0 = e^{-\alpha l} \tag{3}$$

where $I_0$ and $I$ are the incident and transmitted radiation intensity of sunlight respectively, and $l$ is the thickness of a medium that the solar beam needs to cross.

It can be seen that the solar radiation intensity never significantly attenuates in the two glass covers, filled air and two sylgard layers because the intensity ratio for them is determined to be very close to 1. However, the intensity ratio is nearly zero across the silicon layer, implying the solar beam absorbing in that layer due to the doped silicon layer which possesses a very large absorption coefficient. Consequently, the coefficient plays a key role in raising the temperature of the silicon layer.

Experimental evident for the highest temperature core in the silicon layer of a PV cell can be found in [24], where the temperature on the top surface of a flat PV panel and the temperature in the p-n diode junction in the solar cell in the panel were measured simultaneously in laboratory under various radiation intensities in a range of 600–1000 W/m$^2$. It is clarified that the junction temperature in the cell is significantly higher than the surface temperature, for instance, it can be as high as 43 °C above the temperature on the top surface. The other related evidence is found in [25] as well. It is identified that the directly measured temperature in the solar cell of a PV panel always is higher by 4.8 °C than the average temperature of both the top and back surfaces of the panel [25], suggesting the cell temperature should be higher than the temperature either on the top surface or on the bottom surface of the panel.

### *3.7. Predicted optical efficiency and concentration ratio*

The optical concentration ratio, *CR*, is predicted and illustrated in Fig. 10(a). The ratio is calculated based on the extracted wall irradiation intensities on the top glass cover and the bottom surface of Sylgard1 layer. In the figure, the design and measured optical concentration ratios at the 0° incidence in [3] are also provided. As shown, the concentration ratios at 0° are very consistent with each other.

The optical efficiency of a CCPC, $\eta_{opt}$, is defined as the ratio of the product of the wall irradiation flux extracted from the CFX results and the CCPC outlet aperture area to the total solar energy on the top glass cover. A comparison of the experimental and estimated optical efficiency is demonstrated in Fig. 10(b). The efficiency curve given by the CFX results is in good agreement with the measurement.

The comparisons above suggest that the coupled numerical simulations with CFX are reasonable, effective and accurate in optical concentration ratio and efficiency predictions.

## 4. Limitations

The present work is subject to a few limitations. Firstly, as a first trial, we have analysed an isolated CCPC with PV cell rather than a CCPC module or a panel. We therefore do not consider the isolated CCPC's location within a PV module, and the natural convective heat transfer around a CCPC in the centre may differ from that around a CCPC in the corners of a PV module. Actually, the boundary conditions between the two CCPCs or in a corner in a PV module differ from those in the isolated CCPC. In the paper, we have just applied a natural convective heat transfer condition in our experiments and CFD simulations around the isolated CCPC. As a result, the heat loss through the isolated CCPC walls might be higher than the loss through the walls of a CCPV in the PV module. This suggests that our experimental and numerical results can overestimate the heat loss through the CCPC walls. Nonetheless, the effects of this difference in boundary condition on the thermal performance of CCPC need to be investigated in a future study.

Secondly, the grey model is adopted in the work and the optical and thermal results are reasonably consistent with corresponding observations. However, the spectral optical and thermal results are still worthy being studied in the future because the solar radiation intensity depends on wavelength.

Thirdly, in ANSYS CFX, transparent glass is regarded as an opaque body. How to simulate radiative heat transfer in a transparent body with ANSYS CFX is worthy of being tackled in the future.

Lastly, the electrical performance of a PV cell is excluded in the work. The performance is related to the physical parameters and temperature of a doped silicon layer. The electrical performance is coupled with the optical and thermal performance of CCPC with solar cell through the Joule heat generated by wire fingers embedded in the doped silicon layer and the layer itself. This coupling

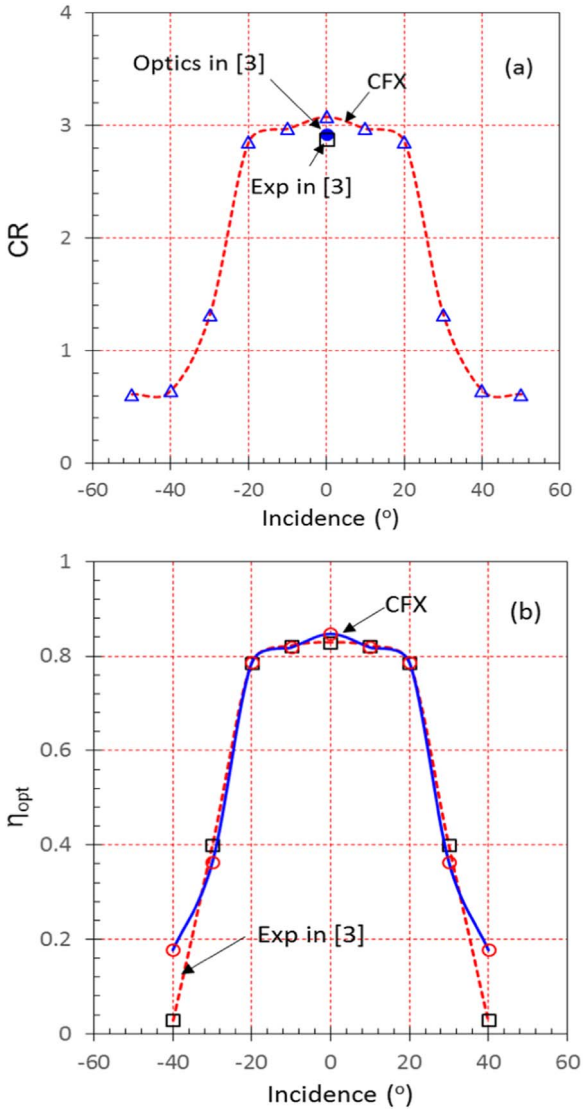


**Fig. 10.** Optical concentration ratio (*CR*) (a) and optical efficiency (b) are showed in terms of incidence, the optical efficiency and *CR* are the measured data for a 3 × 3 CCPC module in [3].

effect needs to be evaluated quantitatively in the future.

## 5. Conclusions

The natural convective heat transfer phenomenon in an isolated, walled CCPC with PV cell is investigated numerically and experimentally under indoor condition at 1000 W/m$^2$ irradiance and 28.5 °C ambient temperature as well as 0°, 10°, 20°, 30° and 40° incidences. The temperature contours on the top glass cover, CCPC walls, sylgard layers, PV cell and bottom glass cover, the velocity patterns in the air-filled enclosure of CCPC are obtained, the Nusselt numbers between the air-filled and its surrounding solid boundaries are extracted. The heat loss ratios from the CCPC walls to the ambient air are estimated from experimental data and ANSYS CFX heat transfer results. It is found that the PV cell is subject to the highest temperature at an incidence less than 20°, otherwise the top glass cover is in the highest temperature. The predicted temperatures, Nusselt numbers and heat loss ratios are basically in agreement with the experimental observations. The optical parameters predicted agree very well with the measurements. The heat loss from the CCPC walls accounts for nearly 60% of the total incoming solar irradiance and significant attention should be paid to it in the design of CCPC. The further work includes numerical simulation and experimental study on natural convective heat transfer in CCPC modules, multi-band optical model and coupled PV cell electrical model.

**Acknowledgement**

The work was supported by EPSRC SUPERGEN Solar Challenge with grant: EP/K022156/1-SUNTRAP.

## Appendix A: The governing equations of optics, heat transfer and fluid flow

*1. Radiation transport in medium*

The sunlight is electromagnetic wave with a spectrum and can travel in any kinds of medium and be described by the Maxwell's equations. A walled CCPC with PV cell can absorb, emit and scatter the sunlight during its propagation. For a plane-parallel medium, the monochromatic radiation intensity of a sunlight beam obeys the following equation along its travel path $s$[28],

$$\frac{1}{\lambda_\nu(s)}\frac{dI_\nu(\mathrm{r},s)}{ds} + I_{\nu b}(\mathrm{r},s) = S_\nu(s) \tag{A1a}$$

where

$$S_\nu(s) = (1-\omega_\nu)I_{\nu b}(T) + \frac{1}{4\pi}\omega_\nu \int_{4\pi} dI_\nu(\mathrm{r},s')\Phi(\mathrm{s}\bullet\mathrm{s}')d\Omega' \tag{A1b}$$

$$\lambda_\nu(s) = \alpha_\nu(s) + \gamma_\nu(s) \tag{A1c}$$

$$\omega_\nu = \frac{\gamma_\nu(s)}{\lambda_\nu(s)} \tag{A1d}$$

$$I_{\nu b}(T) = \frac{2\,m\,\nu^3}{c^2\left[\exp\left(\frac{m\nu}{\varkappa T}\right)-1\right]} \tag{A1e}$$

where $S_\nu(s)$ is the spectral source function, $\lambda_\nu(s)$ is the spectral extinction coefficient, $\alpha_\nu$ is the absorption coefficient of medium, $\gamma_\nu$ is the scattering coefficient of medium, $\omega_\nu(s)$ is the spectral diffuse reflectivity that is a ratio of the scattering coefficient to the extinction coefficient, $m$ and $\varkappa$ are the Planck and Boltzmann constants respectively, $c$ is the speed of sunlight in the medium, $\nu$ is the frequency, $T$ is the absolute temperature, r is the position vector, s is the direction vector, $s$ is the ray path length, $I_{\nu b}(T)$ is the blackbody emission intensity, $I_\nu(\mathrm{r},s)$ is the spectral radiation intensity, $\Omega$ is the solid angle, and $\Phi$ is the scattering phase function.

In this study, we assume the medium to be grey and homogenous without any scattering reflection. Thus, the radiative properties of the medium are independent of frequency or wavelength, path length and $\gamma_\nu = \omega_\nu = 0$. Eventually, Eq. (A1a) is integrated over all frequencies, yielding

$$\frac{1}{\kappa}\frac{dI(\mathrm{r},s)}{ds} + I(\mathrm{r},s) = I_b(T) \tag{A2a}$$

with

$$I(\mathrm{r},s) = \int_{\nu=0}^{\infty} I_\nu(\mathrm{r},s)\,d\nu \tag{A2b}$$

$$\int_{\nu=0}^{\infty} I_{\nu b}(T)d\nu = I_b(T) = \frac{n^2\sigma T^4}{\pi} \tag{A2c}$$

where $\alpha$ is the average absorption coefficient of the medium, $I_b(T)$ is the total blackbody radiation intensity, $\sigma$ is the Stefan-Boltzmann constant, and $n$ is the refractive index of the medium assumed to be independent of frequency. The solar radiation transport behaviour through all the media of the CCPC with PV cell shown in Fig. 1(d) is obtained by solving Eq. (A2a) with the Monte Carlo method.

*2. Radiation transport on interface*

When a beam of sunlight travels through multiple media, it experiences the interfaces between any two media. On the interfaces, the sunlight may be reflected and refracted. For an interface which is subject to an ideal surface i.e. a surface which is optically smooth and perfectly clean as well as without diffuse reflections, the ratio of radiation intensity of the reflected beam over that of the incident beam can be treated analytically by the Maxwell theory. Besides, it is supposed that there are no scattering particles in the media, and the media are dielectric.

Let us consider a beam of sunlight is incident upon the interface between medium 1 and medium 2 as shown Fig. A1. As a result, one beam is reflected at the bottom to medium 1 with an angle $\theta_1$, and is refracted into medium 2 with an angle $\theta_2$. The two components of polarization of electrical field of the beam reflected are determined by the Fresnel's reflection equations written as [29]

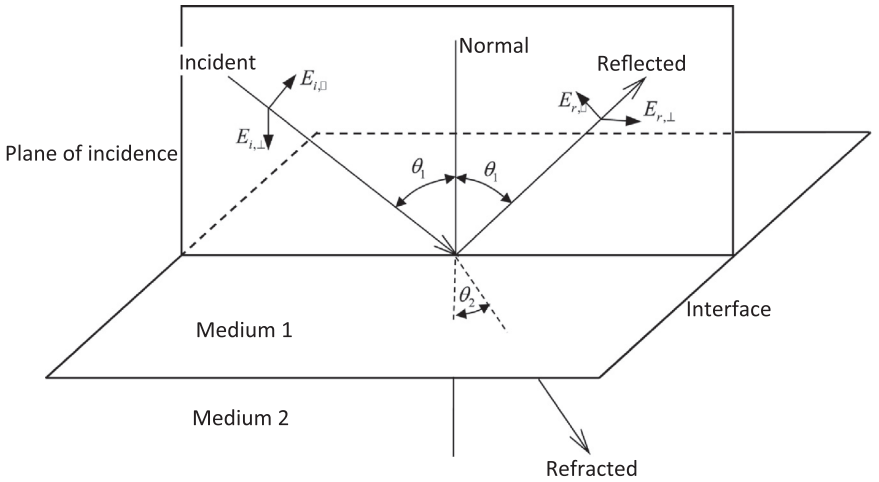


**Fig. A1.** A beam with initial intensity components, $E_{i,\|}$ and $E_{i,\perp}$, is reflected and refracted at the interface between medium 1 and medium 2.

$$\begin{cases} \frac{E_{r,\perp}}{E_{i,\perp}} = -\frac{\sin(\theta_1-\theta_2)}{\sin(\theta_1+\theta_2)} \\ \frac{E_{r,\|}}{E_{i,\|}} = \frac{\tan(\theta_1-\theta_2)}{\tan(\theta_1+\theta_2)} \end{cases} \tag{A3}$$

where $E_{i,\perp}$ and $E_{i,\|}$ denote the two components of the incident beam, one is perpendicular to and the other is parallel to the plane of incidence, likewise, $E_{r,\perp}$ and $E_{r,\|}$ represent those of the reflected beam. The ratio of radiation intensity of the reflected beam over that of the incident beam for the components is defined as

$$\begin{cases} \varsigma_{\nu,\perp} = \left(\frac{E_{r,\perp}}{E_{i,\perp}}\right)^2 = \frac{\sin^2(\theta_1-\theta_2)}{\sin^2(\theta_1+\theta_2)} \\ \varsigma_{\nu,\|} = \left(\frac{E_{r,\|}}{E_{i,\|}}\right)^2 = \frac{\tan^2(\theta_1-\theta_2)}{\tan^2(\theta_1+\theta_2)} \end{cases} \tag{A4a}$$

where $\varsigma_{\nu,\perp}$ and $\varsigma_{\nu,\|}$ are the reflectivity of the two components at frequency $\nu$, respectively. In CFX, however, the radiation is considered to be unpolarised and two components are subject to an equal intensity, thus the reflectivity is the average of $\varsigma_{\nu,\perp}$ and $\varsigma_{\nu,\|}$, namely,

$$\varsigma_\nu = \tfrac{1}{2}(\varsigma_{\nu,\perp} + \varsigma_{\nu,\|}) = \frac{1}{2}\left[\frac{\sin^2(\theta_1-\theta_2)}{\sin^2(\theta_1+\theta_2)} + \frac{\tan^2(\theta_1-\theta_2)}{\tan^2(\theta_1+\theta_2)}\right] \tag{A4b}$$

The ratio of radiation intensity of the refracted beam over that of the incident beam can now be expressed as

$$\varepsilon_\nu = 1 - \varsigma_\nu \tag{A4c}$$

where $\varepsilon_\nu$ is the emissivity or absorptivity of a medium. We have redeemed the grey model above, so that $\varsigma_\nu$ and $\varepsilon_\nu$ are independent of frequency, and hence denoted by $\varsigma$ and $\varepsilon$ respectively.

The angle of refraction $\theta_2$ is determined by using the Snell's law of refraction as below

$$\frac{\sin\theta_2}{\sin\theta_1} = \frac{n_1}{n_2} \tag{A4d}$$

in which $n_1$ and $n_2$ are the refractive index of media 1 and 2 respectively. Ray trace analysis is performed in CFX to track the path of the sunlight beam travelling through the interfaces.

### *3. Fluid flow model*

The density of the air filled in the CCPC cavity or enclosure varies from the PV cell surface to the top glass cover because of the temperature gradient between them. Consequently, the filled air is put into motion in the cavity by the gravity. This upward air current can convey the heat generated from the solar cell surface to the top glass cover, eventually this part of heat is dissipated to the environment. It is shown that the Reynolds number of the CCPC is less than 100 determined based on the maximum air velocity at zero incidence, thus suggesting the filled air flow is laminar. Additionally, under a particular sunlight radiation with a constant environment temperature, the air flow can achieve a steady state. Thus it is plausible to consider the filled air flow to be steady-state and 3D laminar. In a stationary reference frame, the instantaneous continuity, momentum and thermal energy equations can be written as [29]:

$$\frac{\partial \rho}{\partial t} + \nabla \bullet (\rho \vec{U}) = 0 \tag{A5a}$$

$$\frac{\partial (\rho \vec{U})}{\partial t} + \nabla \bullet (\rho \vec{U} \otimes \vec{U}) = -\nabla p + \nabla \bullet \tau + \vec{F} \tag{A5b}$$

$$\frac{\partial (\rho e)}{\partial t} + \nabla \bullet (\rho \vec{U} e) = \nabla \bullet (kT) + \tau : \nabla \vec{U} + S_E \tag{A5c}$$

where $\rho$, $\vec{U}$, $p$, $\tau$, $\vec{F}$, $e$, $T$, $k$ and $S_E$ are the density, velocity, pressure, shear stress tensor, body force, internal energy, temperature, heat conductivity and energy source of air, respectively, and the energy source term $S_E$ is zero. Here the body force $\vec{F}$ takes into account the buoyancy force, i.e.

$$\vec{F} = (\rho - \rho_{ref})\vec{g} \tag{A5d}$$

where $\rho_{ref}$ is the reference density of air at a reference temperature $T_{ref} = 25\ ^{\circ}C$. Since the temperature difference across a CCPC is small, the Boussinesq model is adopted to calculate the density difference, $\rho - \rho_{ref}$, namely

$$(\rho - \rho_{ref}) = -\rho_{ref}\beta(T - T_{ref}) \tag{A5e}$$

where $\beta$ is the thermal expansion of air, and defined as

$$\beta = -\frac{1}{\rho}\frac{\partial p}{\partial T}\bigg|_p \tag{A5f}$$

Note that in the Boussinesq model, a constant reference density $\rho_{ref}$ is applied into all terms in the continuity and momentum equations except in the body force $\vec{F}$. In addition, the pressure in the momentum equations excludes the hydrostatic gradient caused by $\rho_{ref}$. The energy source term $S_E$ is considered to be zero.

Since there is no fluid flow inside the solid domains such as the top glass cover, sylgard and solar cell layers and bottom glass cover, the thermal energy equation, Eq. (A5c), is simplified to the following heat transfer equation

$$\frac{\partial (\rho c_p T)}{\partial t} = \nabla \bullet (\lambda \nabla T) + S_E \tag{A6}$$

where $\rho$, $c_p$ and $k$ are the density, specific heat capacity and thermal conductivity of the solids, respectively; the energy source term $S_E$ is still zero.

The above governing equations are solved sequentially in ANSYS CFX under a set of appropriate boundary conditions until a solution convergence is reached.

## References


[1] T. Cooper, F. Dahler, G. Ambrosetti, A. Pedretti, A. Steinfeld, Performance of compound parabolic concentrators with polygonal apertures, Sol. Energy 95 (2013) 308–318.
[2] E.D. Mammo, N. Sellami, T.K. Mallick, Performance analysis of reflective 3D crossed compound parabolic concentrating photovoltaic system for building faced integration, Prog. Photovolt.: Res. Appl. 21 (2013) 1095–1103.
[3] N. Sellami, T.K. Mallick, Optical efficiency study of PV crossed compound parabolic concentrator, Appl. Energy 102 (2013) 868–876.
[4] B.A. Meyer, J.W. Mitchell, M.M. El-Wakil, Convective heat transfer in vee-trough linear concentrators, Sol. Energy 28 (1982) 33–40.
[5] D.E. Prapas, B. Norton, P.E. Melidis, S.D. Probert, Convective heat transfer within air spaces of compound parabolic concentrating solar-energy collectors, Appl. Energy 28 (1987) 123–135.
[6] A. Fasulo, L. Odicina, D. Perello, Development of a CPC with low thermal losses, Sol. Energy 4 (1987) 157–162.
[7] M. Ronnelid, B. Karlsson, Experimental investigation of heat losses from low-concentrating non-imaging concentrators, Sol. Energy 57 (1996) 93–109.
[8] H. Singh, P.C. Eames, A review of natural convection heat transfer correlations rectangular cross-section cavities and their potential applications to compound parabolic concentrating (CPC) solar collector cavities, Appl. Therm. Eng. 31 (2011) 2186–2196.
[9] H. Singh, P.C. Eames, Correlation for natural convective heat exchange in CPC collector cavities determined for experimental measurements, Sol. Energy 86 (2012) 2443–2457.
[10] T.N. Anderson, Natural convection heat transfer in V-trough solar concentrators, Sol. Energy 95 (2013) 224–228.
[11] P.C. Eames, B. Norton, Validated, unified model for optics and heat transfer in line-axis concentrating solar energy collectors, Sol. Energy 50 (1993) 339–355.
[12] P.C. Eames, B. Norton, Detailed parametric analyses of heat transfer in CPC solar energy collectors, Sol. Energy 50 (1993) 321–338.
[13] P.C. Eames, B. Norton, Y. Tripagnostopoulos, P. Yianoulis, Modelling line-axis solar concentrators in the medium temperature range, Sol. Energy 16 (1999) 743–748.
[14] P.C. Eames, M. Smyth, B. Norton, The experimental validation of a comprehensive unified model for optics and heat transfer in line-axis concentrating solar energy systems, Sol. Energy 71 (2001) 121–133.
[15] T.K. Mallick, P.C. Eames, B. Norton, Using air flow to alleviate temperature elevation in solar cells within asymmetric compound parabolic concentrators, Sol. Energy 81 (2007) 173–184.
[16] T.K. Mallick, P.C. Eames, Electrical performance evaluation of low-concentrating non-imaging photovoltaic concentrator, Prog. Photovolt.: Res. Appl. 16 (2008) 389–398.
[17] S.K. Natarajan, T.K. Mallick, M. Katz, S. Weingaertner, Numerical investigations of solar cell temperature for photovoltaic concentrator system with and without passive cooling arrangements, Int. J. Therm. Sci. 50 (2011) 2514–2521.
[18] P. Horta, J.C.C. Henriques, M. Collares-Pereira, Impact of different internal convection control strategies in a non-evacuated CPC collector performance, Sol. Energy 86 (2012) 1232–1244.

[19] Ch Reichl, F. Hengstberger, Ch Zauner, Heat transfer mechanisms in a compound parabolic concentrator: Comparison of computational fluid dynamics simulations to particle image velocimetry and local temperature measurements, Sol. Energy 97 (2013) 436–446.
[20] E.D. Mammo, N. Sellami, T.K. Mallick, Performance analysis of reflective 3D crossed compound parabolic concentrating photovoltaic system for building faced integration, Prog. Photovolt.: Res. Appl. 21 (2013) 1095–1103.
[21] W.G. Li, M.C. Paul, et al., Coupled simulation of performance of a crossed compound parabolic concentrator with solar cell, Energy Procedia 75 (2015) 325–330.
[22] W.G. Li, M.C. Paul, et al., Experimental and numerical investigation of thermal performance of a crossed compound parabolic concentrator with PV cell, in: Proceedings of the 12th International Conference on Heat Transfer, Fluid Mechanics and Thermodynamics, Malaga, Spain, 2016, pp:911–914.
[23] N. Sarmah, Design and Performance Evaluation of a Low Concentrating Line-axis Dielectric Photovoltaic System (Ph.D. Thesis), Heriot-Watt University, Edinburgh, UK, 2012.
[24] S.H. Jang, M.W. Shin, Thermal characterization of junction in solar cell package, IEEE Electron Device Lett. 31 (2010) 743–745.
[25] B.J. Huang, P.E. Yang, Y.P. Lin, B.Y. Lin, H.J. Chen, R.C. Lai, J.S. Cheng, Solar cell junction temperature measurement of PV module, Sol. Energy 85 (2011) 388–392.
[26] H.P. Garg, R.S. Adhikari, Performance analysis of a hybrid photovoltaic/thermal (PV/T) collectors with integrated CPC troughs, Int. J. Energy Res. 23 (1999) 1295–1304.
[27] H.P. Garg, R.S. Adhikari, Transient simulation of conventional hybrid photovoltaic/thermal (PV/T) air heating collectors, Int. J. Energy Res. 22 (1998) 547–562.
[28] M.N. Ozisik, Radiative Transfer, John Wiley & Sons, New York, 1973.
[29] ANSYS, CFX-Solver Theory Guide, Release 15.0, ANSYS, Inc., Canonsburg, PA, USA, 2013.
[30] K.S. Ong, Thermal performance of solar air heaters: mathematical model and solution procedure, Sol. Energy 55 (2) (1995) 93–109.
[31] J.R. Simonson, Engineering Heat Transfer, MacMillan Press Ltd, London, 1975, pp. 218–221.